

Molecular Signal Reception in Complex Vessel Networks: The Role of the Network Topology

Timo Jakumeit, Lukas Brand, Jens Kirchner, Robert Schober, and Sebastian Lotter
Friedrich-Alexander-Universität Erlangen-Nürnberg (FAU), Erlangen, Germany

Abstract—The notion of synthetic molecular communication (MC) refers to the transmission of information via molecules and is largely foreseen for use within the human body, where traditional electromagnetic wave (EM)-based communication is impractical. MC is anticipated to enable innovative medical applications, such as early-stage tumor detection, targeted drug delivery, and holistic approaches like the Internet of Bio-Nano Things (IoBNT). Many of these applications involve parts of the human cardiovascular system (CVS), here referred to as *networks*, posing challenges for MC due to their complex, highly branched vessel structures. To gain a better understanding of how the topology of such branched vessel networks affects the reception of a molecular signal at a target location, e.g., the network outlet, we present a generic analytical end-to-end model that characterizes molecule propagation and reception in linear branched vessel networks (LBVNs). We specialize this generic model to any MC system employing superparamagnetic iron-oxide nanoparticles (SPIONs) as signaling molecules and a planar coil as receiver (RX). By considering components that have been previously established in testbeds, we effectively isolate the impact of the network topology and validate our theoretical model with testbed data. Additionally, we propose two metrics, namely the *molecule delay* and the *multi-path spread*, that relate the LBVN topology to the molecule dispersion induced by the network, thereby linking the network structure to the signal-to-noise ratio (SNR) at the target location. This allows the characterization of the SNR at any point in the network *solely based on the network topology*. Consequently, our framework can, e.g., be exploited for optimal sensor placement in the CVS or identification of suitable testbed topologies for given SNR requirements.

I. INTRODUCTION

The concept of synthetic molecular communication (MC) stands in contrast to traditional electromagnetic wave (EM)-based communication and refers to the transmission of information via signaling molecules. The primary application domain of MC is the human body, where the liquid environment impedes EM-based communication between nanoscale devices owing to poor signal propagation conditions. Here, MC is anticipated to facilitate the development of innovative medical procedures by enabling the exchange of information between biological and synthetic systems.

Many in-body applications are envisioned to operate in the cardiovascular system (CVS), which serves as a central distribution network within the body. Examples include tumor detection, whereby the presence of cancerous tissue is detected by nanosensors that measure elevated concentrations of biomarkers in the vicinity of the tumor [1]. Similarly, tumor targeting involves functionalized nanoparticles that target the diseased region and deliver drugs for the destruction of malicious cells, thereby minimizing adverse side effects elsewhere in the body [2]. Another example is the Internet of Bio-Nano Things (IoBNT), in which gateways receive molecular information inside the body, e.g., along the CVS, and then transmit the information via EM signals to an external computational unit, which performs processing and evaluation. These gateways work bidirectionally, i.e., they can also receive

EM signals from the computational unit and convert them into a molecular signal for internal transmission, thereby seamlessly integrating both communication paradigms to enable, e.g., health monitoring and personalized treatment [3].

The implementation of such applications is challenging due to the highly branched nature of the CVS, which comprises vessels, *bifurcations* (one vessel splitting up into multiple vessels), and *junctions* (multiple vessels joining into one), resulting in complex dynamics of signaling molecule transport. To gain a deeper understanding of molecule propagation in the CVS, several theoretical studies have been conducted. In [4], a channel model for branched vessel structures based on channel impulse responses (CIRs) is proposed. The authors focus on molecule propagation in arterial tree structures, i.e., on bifurcations, with less consideration given to vessel junctions. A method for early cancer detection that uses mobile nanosensors traversing the CVS is introduced in [1]. The model is developed under the assumption of a quasi-steady state signaling molecule concentration, which in many systems is not applicable due to the time variance of the molecule release. In [5], a framework for estimating the required dosage of cellular vaccines injected into the CVS for treatment of COVID-19 is presented. While the model accounts for propagation in branched topologies, only individual branchings are analyzed. References [1], [4], [5] highlight the lack of a 'network-wide' view of MC. In particular, an abstract understanding of the impact that the network structure has on communication is missing in the literature. Along similar lines, the experimental MC literature has repeatedly demonstrated the feasibility of communication via various signaling molecules in testbeds with simple channel structures such as single pipes or bifurcations [6]–[8]. However, only very few testbeds with highly branched network topologies, reminiscent of those found in the CVS, exist [9], [10].

To address these knowledge gaps, we here propose a generic analytical end-to-end model for the transport and reception of arbitrary signaling molecules in linear branched vessel networks (LBVNs). Assuming particle transport can be characterized by linear systems and consequently CIRs, LBVNs approximate complex vessel networks like the CVS [4]. In particular, we extend the channel model in [4] to account for turbulent diffusion at the network branching points, and link it to a transparent receiver (RX) model. Our primary focus is the investigation of the effects that the LBVN topology exerts on the signal received at the outlet of the network. We specialize the generic model to superparamagnetic iron-oxide nanoparticles (SPIONs) as information carriers [11] and introduce a novel statistical model for reception via a planar coil RX. These components, well established in previous testbeds [6], [8], harbor fundamentally fewer uncertainties compared to biological testbeds, e.g., based on fluorescent proteins or bacteria, allowing us to effectively isolate the impact of the topology. Leveraging the generic model, we devise new metrics—namely the *molecule delay*

and the *multi-path spread*—that relate the topology of any LBVN to the degree of molecule dispersion induced by the network. The degree of dispersion is in turn related to the signal-to-noise ratio (SNR) of the signal received at the outlet of the network, enabling the characterization of the SNR of any LBVN *solely based on its topology*. In this manner, the proposed framework can be exploited to determine the optimal placement of sensors with certain SNR requirements within highly branched vessel networks, such as the CVS, or to predict the structural complexity allowed in testbeds to ensure sufficient signal strength at the RX.

The remainder of this paper is structured as follows: Section II provides the generic system model, which is specialized to a SPION-based MC system in Section III. Building on this, Section IV derives metrics that relate the topology of LBVNs to the SNR at the RX. The model is validated with testbed data and the impact of the topology of LBVNs is studied in Section V. Final conclusions are presented in Section VI.

II. SYSTEM MODEL

In this section, we introduce a system model for the molecule release, i.e., the injection process, at the transmitter (TX), molecule propagation in the channel, and a transparent RX, cf. Fig. 1a). The system model is generically applicable to different types of signaling molecules and the corresponding transparent RX architectures. In Section III, the system model is specialized for the use of SPIONs as information carriers.

A. Molecule Injection

At time $t = 0$ s, N signaling molecules are injected instantaneously by the TX, i.e., the inlet of the network at longitudinal coordinate $z = 0$ m of the corresponding vessel, cf. Fig. 1a). In practical systems, the injection via a Y-connector or venous cannula induces local turbulence in the fluid flow [7], which results in the immediate radial dispersion of the signaling molecules. Accordingly, we postulate a uniform distribution of signaling molecules throughout the pipe cross-section from the moment of injection onwards. The accuracy of this assumption is verified by the numerical results presented in Section V-A.

B. Linear Branched Vessel Networks

Branched systems, such as the CVS, generally exhibit complex topologies, comprising interconnected vessels of varying length, curvature, and irregular cross-sections. To facilitate analysis, these networks are often approximated using simplified models for their segments [1], [4], [5]. Accordingly, we here consider LBVNs consisting of E connected pipes, bifurcations, and J junctions, as illustrated in Fig. 1a).

- 1) *Pipe*: A pipe p_i is a cylindrical vessel carrying fluid from its inlet to its outlet and is defined by its length l_i and radius r_i . Pipes can be connected to other pipes, bifurcations or junctions at both the inlet and the outlet.
- 2) *Bifurcation*: A bifurcation is a connection point with no spatial extent, where an inflow pipe branches into several outflow pipes. Before and after each bifurcation, there must be connected pipes.
- 3) *Junction*: A junction j_m is a connection point with no spatial extent, where several inflow pipes merge into one outflow pipe. Before and after each junction, there must be connected pipes. We denote the set of all inflow pipes of junction j_m by $\mathcal{I}(j_m)$.

Subsequently, we refer to the network inlet, outlet, and connection points, i.e., bifurcations and junctions, as nodes n_v , $v \in \{1, \dots, V\}$, where V is the total number of nodes, and n_1 and n_V are the nodes at the network inlet and outlet, respectively. Pipes correspond to directed edges between these nodes, with the direction of the edge determined by the flow direction. This allows for a simplified representation of any LBVN as a directed graph, as depicted with blue nodes and white arrows in Fig. 1a) for an exemplary network. In addition, $\mathcal{P}(n_a, n_b)$ denotes the set of all paths between nodes n_a and n_b that differ in at least one pipe, with $a, b \in \{1, \dots, V\}$. Here, a path P_k comprises a subset of connected pipes and junctions of the network and is denoted as

$$P_k = \{p_i \mid i \in E_k\} \cup \{j_m \mid m \in J_k\}, \quad (1)$$

where $E_k \subseteq \{1, \dots, E\}$ and $J_k \subseteq \{1, \dots, J\}$ are the index sets of the pipes and junctions in P_k , respectively. Bifurcations are implicitly accounted for in $\mathcal{P}(n_a, n_b)$, as they determine which paths exist.

C. Molecule Transport

We restrict our model to advection-diffusion-based MC. The flow rate Q applied at the inlet gives rise to a background flow in all pipes of the network. While laminar flow prevails under typical conditions in the CVS when considering *individual pipes* [7], a fundamentally different flow behavior is associated with LBVNs. Here, turbulences at the injection site and connection points, like bifurcations and junctions, are expected to extend into the connected pipes, causing turbulent mixing throughout the majority of the highly branched network (cf. lower left part of Fig. 1a). As a result, molecules are expected to be well-mixed in the cross-section at all times, permitting a (spatially) one-dimensional model for molecule transport [4]. While modeling individual turbulences is intractable, a simple way to represent this type of molecular transport is by assuming underlying laminar flow in conjunction with eddy diffusion, represented by the eddy diffusion coefficient [12, Eq. (4.16)]

$$K_i = \alpha \bar{u}_i r_i, \quad \alpha \in [0, 2]. \quad (2)$$

Here, α denotes a unitless proportionality constant. In a given pipe p_i , K_i is proportional to the distance orthogonal to the flow direction over which eddies persist, which is proportional to the pipe radius r_i and flow velocity \bar{u}_i [12]. The latter is obtained as follows: For the typical parameters of the CVS, see Section III-A, the model operates in the Aris-Taylor regime [13]. This allows to simplify the modeling of the advection-diffusion process by averaging the radially dependent flow velocity inside any pipe p_i to a one-dimensional cross-sectional average velocity \bar{u}_i , obtained from equivalent electrical circuits via node voltage analysis, see Fig. 1b) (for details see [4]). The corresponding flow rate in p_i is given as $Q_i = \bar{u}_i \pi r_i^2$.

Besides this, molecules disperse due to molecular diffusion, characterized by the molecular diffusion coefficient [4, Eq. (44)]

$$D = \frac{k_B T}{6\pi\mu R}, \quad (3)$$

where $k_B = 1.38 \times 10^{-23} \text{ m}^2 \text{ kg s}^{-2} \text{ K}^{-1}$, T , μ , and R denote the Boltzmann constant, the fluid temperature, the dynamic fluid viscosity, and the molecule radius, respectively. Molecular and eddy diffusion can be modeled as additive phenomena and are both incorporated in the total diffusion coefficient

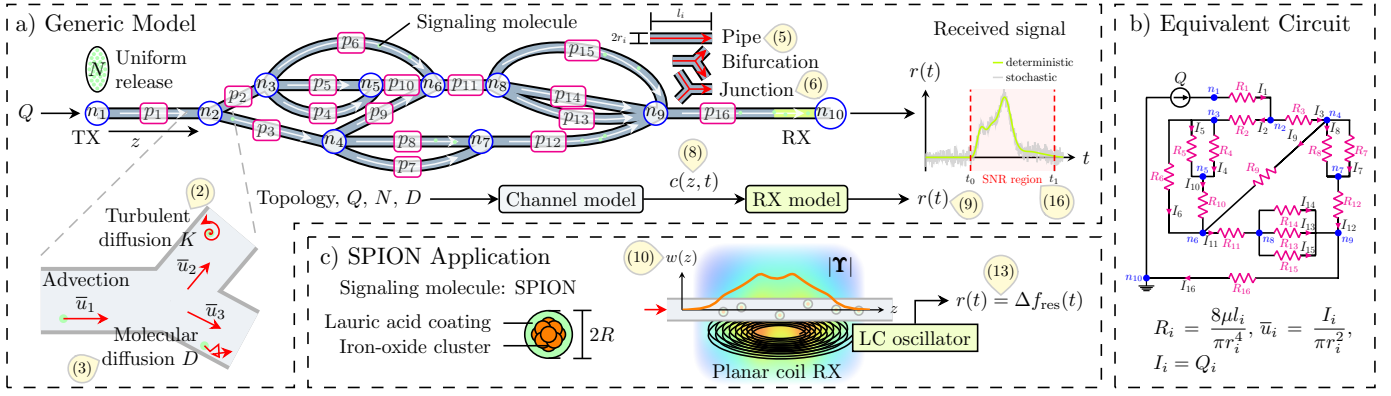


Fig. 1: System model: a) N signaling molecules are uniformly released in the cross-section of the network inlet (TX), propagate through an LBVN comprised of pipes, bifurcations, and junctions by advection as well as molecular and turbulent diffusion, and are received by a transparent RX. b) The cross-sectional average flow velocity \bar{u}_i in pipe p_i is determined using an equivalent electrical circuit that models hydraulic resistance. c) SPIONs as signaling molecules are received by a planar coil connected to an LC oscillator, yielding resonance frequency shift $\Delta f_{\text{res}}(t)$ as received signal. The magnetic field around the coil is nonuniform and captured by the weighting function $w(z)$. Detailed explanations of the system components and notation are provided in the text, relevant equations are marked in yellow in the figure.

$D_i^{\text{tot}} = D + K_i$. Lastly, the Aris-Taylor effective diffusion coefficient is given as [13, Eq. (26)]

$$D_i^{\text{eff}} = \frac{r_i^2 \bar{u}_i^2}{48 D_i^{\text{tot}}} + D_i^{\text{tot}}. \quad (4)$$

On the basis of the above models, molecule transport in LBVNs can be described using CIRs, as illustrated in [4]¹. Specifically, a CIR can be derived for each of the three types of channel segments. Under the assumption of linearity, the end-to-end network CIR then results from the convolution and superposition of corresponding segment CIRs.

Solving the advection-diffusion equation results in the CIR of pipe p_i [4, Eq. (49)]

$$h_i(z, t) = \frac{1}{\sqrt{4\pi D_i^{\text{eff}} t}} \exp\left(-\frac{(z - \bar{u}_i t)^2}{4 D_i^{\text{eff}} t}\right), \quad t > 0, z \in [0, l_i], \quad (5)$$

where z denotes the longitudinal coordinate *within the pipe*, i.e., reaching from its inlet at $z = 0$ to its outlet at $z = l_i$. The principle of mass conservation yields the CIR of a junction j_m that is traversed through p_i [4, Eq. (52)]

$$h_m^i(t) = \frac{\bar{u}_i}{\sum_{k \in \mathcal{I}(j_m)} \bar{u}_k} \delta(t), \quad (6)$$

i.e., molecules partition according to the ratio of flow velocities². Here, $\delta(\cdot)$ denotes the Dirac delta function. The end-to-end CIR of the network between n_a and n_b equals the sum of the individual path CIRs, which in turn result from the convolution of the CIRs of the segments comprising the path [4, Eq. (66)]

$$h_{n_a, n_b}(z, t) = \left[\sum_{P_k \in \mathcal{P}(n_a, n_b)} \left(\bigotimes_{\substack{p_i \in P_k \\ p_i \neq p_{i'}}} h_i(l_i, t) \bigotimes_{\substack{j_m \in P_k \\ p_i \in \mathcal{I}(j_m)}} h_m^i(t) \right) \right] * h_{i'}(z, t), \quad (7)$$

where $*$ (\bigotimes) denotes the convolution operator (over a set) with respect to t , and $p_{i'}$ denotes the pipe containing the RX. Since molecule concentration remains unchanged across bifurcations [4, Eq. (53)], their CIRs do not appear in (7). From (7), the received molecule concentration in unit m^{-3} is obtained as

$$c(z, t) = N h_{n_a, n_b}(z, t). \quad (8)$$

¹Note that [4] does not account for eddy diffusion.

²The fraction was incorrectly inverted in [4]; we present a corrected version.

D. Molecule Reception

We consider a transparent RX whose domain extends over z . The generic received signal results from the concentration as

$$r(t) = f\left(\int_{z \in \text{dom}(w(\cdot))} w(z) c(z, t) dz\right), \quad (9)$$

where $\text{dom}(\cdot)$ denotes the domain operator. Here, weighting function $w(z)$ and signal conversion function $f(x)$ are specific to the sensor employed as RX. Thereby, potential inhomogeneities of the sensing process³ over z are captured by $w(z)$ and subsequent processing steps⁴ are mapped by $f(x)$.

In the MC literature, often the special case of a so-called perfect counting RX, extending from z^- to z^+ with $w(z) = 1$, $\forall z \in [z^-, z^+]$, and linear mapping, i.e., $f(x) = x$, is assumed. In this case, the received signal equals the number of observed molecules $N^{\text{obs}}(t) = \int_{z^-}^{z^+} c(z, t) dz$. In practice, however, sensors with such properties do not exist, emphasizing the need for the sensor-related degrees of freedom in (9).

III. SPION TRANSPORT AND RECEPTION

In this section, we describe how the system model introduced above can be adapted to SPION-based MC. To this end, we first present the physical parameters of SPIONs and derive the resulting transport properties. Secondly, a novel analytical model for the reception process using a planar coil is proposed.

A. Information Carriers

SPIONs are superparamagnetic nanoparticles, e.g., synthesized through co-precipitation [11]. At their core, they hold a cluster of iron-oxide molecules, responsible for a high magnetic susceptibility $\chi_{\text{ref}} \approx 3 \times 10^{-3}$ (SI units) [7]. As a result, SPIONs become strongly magnetized in the presence of an external magnetic field, but show no remanence once removed from the field, due to their small size [6]. Various coatings can be applied to the core, including biocompatible coatings like human serum albumin, chemical degradation and agglomeration mitigating coatings like Dextran, therapeutic coatings carrying

³Consider, e.g., optical RXs in the CVS where varying refractive indices of surrounding tissue cause sensing inhomogeneities over space.

⁴Consider, e.g., differential RXs where the current measured signal amplitude is compared to that measured in previous time steps or a reference signal.

drug particles, or ligands that bind to desired target sites [11]. Depending on the coating, the diameters of SPIONs range from below 10 nm to micrometers [11]. In the following, we consider SPIONs with a lauric acid coating for chemical stability and biocompatibility having a radius of $R = 24.5$ nm [7].

B. Diffusion

For an assessment of the dynamic properties of SPIONs, consider the following scenario. To enable comparison with testbed data, hereafter we assume that the molecules are suspended in distilled water at room temperature $T = 293$ K with $\mu = 1 \times 10^{-3}$ kg m $^{-1}$ s $^{-1}$. This results in a molecular diffusion coefficient $D \approx 8.61 \times 10^{-12}$ m 2 s $^{-1}$, cf. (3). Typical medium-sized arteries in the human CVS, e.g., in the index finger, exhibit a radius in the order of $r \approx 6.5 \times 10^{-4}$ m and an average flow velocity around $\bar{u} \approx 5 \times 10^{-2}$ m s $^{-1}$ [14]. According to (2), this yields a maximum eddy diffusion coefficient of $K \approx 3.25 \times 10^{-5}$ m 2 s $^{-1} \gg D$ for $\alpha = 2$. As the exact value of α can typically only be obtained experimentally, in Section V-A, we fit α to testbed data from [6]. Lastly, utilizing (4) yields a maximum effective diffusion coefficient of $D^{\text{eff}} \approx 3.32 \times 10^{-5}$ m 2 s $^{-1}$ ($\alpha = 2$).

C. Planar Coil Receiver

Due to their magnetic properties, SPIONs can be detected using capacitive and inductive RXs. In this work, we model the inductive RX used in the testbed in [6]. The testbed comprises a straight channel pipe, molecule injection via a venous cannula, and a planar coil RX⁵ with a connected LC oscillation circuit. Unlike conventional cylindrical coils, planar coils can be positioned adjacent to the vessels, eliminating the need to envelop them, cf. Fig. 1c). When SPIONs enter the vicinity of the coil, a cascade of physical processes leads to the detection of the molecules through the oscillator, as detailed in the following.

1) *Magnetic Susceptibility*: In the presence of SPIONs, the volume magnetic susceptibility χ_v (unitless) of the environment increases, since water and air exhibit much lower susceptibilities compared to the nanoparticles. Given that the magnetic field around planar coils is non-homogeneous, cf. Fig. 1c), different SPIONs contribute differently to the received signal, depending on their position. In particular, their contribution is proportional to the strength of the magnetic field⁶, denoted by $|\mathbf{T}(z)|$, which we capture using the unitless weighting function [7]

$$w(z) = \beta \chi_{\text{ref}} |\mathbf{T}(z)|, \quad (10)$$

where β denotes a proportionality constant. Since closed-form expressions for the magnetic field strength can only be found for simple coil geometries, we obtain $|\mathbf{T}|$ through COMSOL[®] simulations⁷. Subsequently, volume magnetic susceptibility $\chi_v(t)$ is obtained from the integral in (9), i.e., $\chi_v(t) = \int_{z \in \text{dom}(w(\cdot))} w(z) c(z, t) dz$, using the weighting function in (10).

2) *Inductance*: A change in $\chi_v(t)$ in turn implies a change in the coil inductance

$$L(t) = \mu_r(t) L_0 = (1 + \chi_v(t)) L_0, \quad (11)$$

⁵The testbed employs coil "K" from the LDCCOILEVM reference coils board by Texas Instruments, cf. <https://www.ti.com/tool/LDCCOILEVM>.

⁶For simplicity, we assume the RX pipe diameter is small enough, such that all SPIONs at a given z experience the same magnetic field strength.

⁷For the simulation file, see <https://doi.org/10.5281/zenodo.13744883>.

where $\mu_r(t)$ is a unitless quantity denoting the relative permeability and L_0 denotes the coil inductance when no SPIONs are in the proximity. COMSOL simulations⁷ yield $L_0 = 206.51$ μH , which is very close to the value $L_0 = 206.227$ μH reported by the coil manufacturer, which we use in the following.

3) *Resonance Frequency Shift*: The LC oscillation circuit in [6] employs a capacitor with capacitance $C = 68$ pF and resonates at frequency

$$f_{\text{res}}(t) = \frac{1}{2\pi \sqrt{L(t)C}}. \quad (12)$$

Let $f_{\text{res},0}$ denote the resonance frequency if no SPIONs are near the coil, i.e., for $L(t) = L_0$. Then, we define the deterministic received signal as resonance frequency shift [8, Eq. (1)]

$$\Delta f_{\text{res}}(t) = f_{\text{res}}(t) - f_{\text{res},0} = \frac{\sqrt{L(t)} - \sqrt{L_0}}{2\pi \sqrt{L_0 L(t) C}}. \quad (13)$$

Consequently, complying with the generic framework, the received signal $r(t)$ for SPION-based MC results from (9) with $w(z)$ in (10) and $f(x)$ comprised of (11) – (13).

In practice, the received signal is impacted by noise. To characterize the noise at the planar coil RX, we evaluate the testbed CIRs in [6], measured at varying channel lengths and background flow rates in terms of resonance frequency shift in unit Hz. For each testbed parameter setting, we collect the deviations between ten measured CIRs and their respective ensemble-averaged CIR over time, and analyze the distribution of the deviations. By focusing on a low-signal amplitude time window around the CIR tails, we observe similar signal-independent, additive white Gaussian noise n_{sensor} across all settings, which is accurately modeled as

$$n_{\text{sensor}} \sim \mathcal{N}(\xi = 0 \text{ Hz}, \sigma^2 = 0.3822 \text{ kHz}^2), \quad (14)$$

where $\mathcal{N}(\xi, \sigma^2)$ denotes the Gaussian probability density function with mean ξ and variance σ^2 . This noise, attributed to sensor inaccuracies, is the most prominent noise affecting the data, leading to the statistical received signal model

$$\Delta F_{\text{res}}(t) = \Delta f_{\text{res}}(t) + n_{\text{sensor}}(t), \quad (15)$$

i.e., for any t , $\Delta F_{\text{res}}(t)$ is a random variable. Similar to [15, Eq. (5)], we define a time-average SNR. In particular, for the averaging, we capture the entire received signal, excluding its vanishing onset and tail, cf. right part of Fig. 1a),

$$\text{SNR} = 10 \log_{10} \left(\frac{\frac{1}{t_1 - t_0} \int_{t_0}^{t_1} \Delta f_{\text{res}}^2(t) dt}{\sigma^2} \right), \quad (16)$$

$$t_0 = \sup\{t < t_{\text{first path}} \mid \Delta f_{\text{res}}(t) \leq \epsilon\},$$

$$t_1 = \inf\{t > t_{\text{last path}} \mid \Delta f_{\text{res}}(t) \leq \epsilon\},$$

where $t_{\text{first path}}$ and $t_{\text{last path}}$ denote the first and last path peak times (cf. (18)) in $\Delta f_{\text{res}}(t)$, respectively, and ϵ denotes a small threshold, chosen as $\epsilon = 1$ mHz in our simulations.

IV. TOPOLOGY-DISPERSION METRICS

To characterize how the network topology affects the received molecular signal, below, we propose metrics that relate the topology of LBVNs to the received SNR. In particular, these metrics are derived from the generic system model in Section II and characterize how strongly molecules are dispersed by a given network topology, taking into account molecular and eddy diffusion. The degree of dispersion is in turn associated with the received SNR. This methodology is akin to the characterization

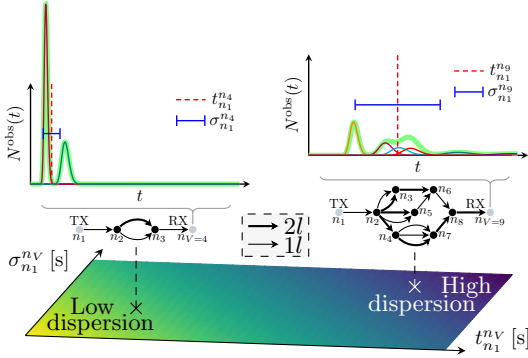


Fig. 2: The position of any LBVN in the dispersion space is solely based on its topology, as $t_{n_1}^{n_V}$ and $\sigma_{n_1}^{n_V}$ characterize the dispersion of the molecules propagating from TX to RX. Two exemplary LBVN with identical pipe radii and pipe lengths of either l or $2l$, along with their received signals $N^{\text{obs}}(t)$, are shown. Thin colored curves show individual path contributions; the green curve shows the total signal.

of multi-path channels in wireless communications, where similar metrics are employed to assess the influence of the channel on the quality of the received signal [16].

1) *Molecule Delay*: The extent of molecule dispersion via diffusion from the network inlet to the outlet is inherently linked to the molecule travel time, with longer delays implying larger dispersion, cf. (5). Our first metric below captures this.

For a single pipe p_i , the time when most molecules are located at its outlet, denoted as the pipe peak time, is given as

$$t_{p_i}^{\text{peak}} = \arg \max_t h_i(l_i, t) = \frac{-D_i^{\text{eff}} + \sqrt{D_i^{\text{eff}2} + \bar{u}_i^2 l_i^2}}{\bar{u}_i^2}. \quad (17)$$

From (17), the time when most molecules are located at the outlet of a path P_k , denoted as the path peak time, follows as

$$t_{P_k}^{\text{peak}} = \sum_{p_i \in P_k} t_{p_i}^{\text{peak}}. \quad (18)$$

Moreover, the fraction of molecules traveling through P_k is

$$\gamma_{P_k} = \prod_{\substack{p_i, j_m \in P_k \\ p_i \in \mathcal{I}(j_m)}} \frac{\bar{u}_i}{\sum_{p_v \in \mathcal{I}(j_m)} \bar{u}_v}, \quad (19)$$

i.e., the product of the flow velocity fractions of all junctions contained in the path. From (17) – (19), we define the *molecule delay* for a given network between nodes n_a and n_b as

$$t_{n_a}^{n_b} = \sum_{P_k \in \mathcal{P}(n_a, n_b)} \gamma_{P_k} t_{P_k}^{\text{peak}}, \quad (20)$$

giving, via γ_{P_k} , more weight to paths carrying more molecules. Note that $t_{n_a}^{n_b}$ resembles the *excess delay* in multi-path wireless communications, quantifying the mean signal delay [16].

2) *Multi-Path Spread*: Secondly, networks with paths having widely varying peak times $t_{P_k}^{\text{peak}}$ lead to increased dispersion, causing molecules to arrive at the RX more spread out over time. We capture this phenomenon by the *multi-path spread*

$$\sigma_{n_a}^{n_b} = \sqrt{\sum_{P_k \in \mathcal{P}(n_a, n_b)} \gamma_{P_k} (t_{P_k}^{\text{peak}} - t_{n_a}^{n_b})^2}. \quad (21)$$

Note that $\sigma_{n_a}^{n_b}$ parallels the *root mean square delay spread*, describing signal spread in a multi-path wireless channel [16].

3) *Dispersion Space*: $t_{n_a}^{n_b}$ and $\sigma_{n_a}^{n_b}$ span a two-dimensional space we term *dispersion space*, cf. Fig. 2. Any LBVN can be located in the space *solely based on its topology*. Setting $n_a =$

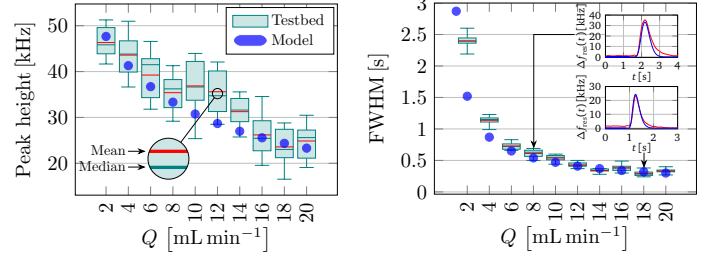


Fig. 3: Comparison of testbed CIRs in [6] and model CIRs at varying flow rates Q in terms of peak height and FWHM.

$n_1, n_b = n_V$, the position in the space can then be used to infer the degree to which molecules disperse while propagating from TX to RX. LBVN close to the origin experience comparatively little dispersion and LBVN far away from the origin suffer from strong dispersion, cf. left and right network in Fig. 2, respectively. Lastly, we hypothesize that the level of dispersion correlates negatively with the received SNR.

V. NUMERICAL EVALUATION

In this section, we validate our end-to-end model with testbed data and subsequently evaluate how the dispersion space can be used to infer the received SNR from the network topology.

A. Comparison to Testbed Data

For the validation of our end-to-end model, we compare the CIRs measured in [6] with those predicted by (13), focusing on CIR peak height and the CIR full width at half maximum (FWHM), cf. Fig. 3. These quantities are crucial for signal reception [6]. We adopt all default parameters from [6, Tab. 1], vary the background flow rate Q for a fixed channel length $l = 5$ cm as done in [6], and estimate $\alpha = 0.076$ and $\beta = 1 \times 10^{-8}$ by fitting our model to the testbed data. In [6], ten CIR realizations are measured for each setting, the statistics of which are illustrated in Fig. 3 using boxplots.

First, we consider the peak heights of the CIRs. Testbed and model data show good agreement, with decreasing peak heights as Q increases. This trend occurs because greater Q imply greater flow velocities and thus stronger effective diffusion, cf. (4), which ultimately leads to molecules being more spread out over space, i.e., less SPIONs are present in the magnetic field of the RX at pipe peak time. The deviations between 10 and 14 mL min^{-1} are likely due to testbed measurement inaccuracies, as these data points significantly deviate from the general trend. Secondly, the model FWHM aligns with the testbed data, decreasing as Q increases because molecules pass through the magnetic field of the RX more quickly at higher Q , resulting in narrower CIRs. Notable deviations for low Q are likely due to channel soiling, which becomes more pronounced in the testbed at low flow velocities and is not accounted for in our model. In summary, these results demonstrate that our model accurately reproduces the testbed data.

B. Dispersion Space

To verify that the received SNR can be directly inferred from the network topology utilizing the proposed dispersion space, we analyze a variety of synthetically generated LBVN. For each of the four template networks shown in Fig. 4a), six further networks are generated by iteratively removing one pipe in the order indicated in color, totaling 28 networks. The

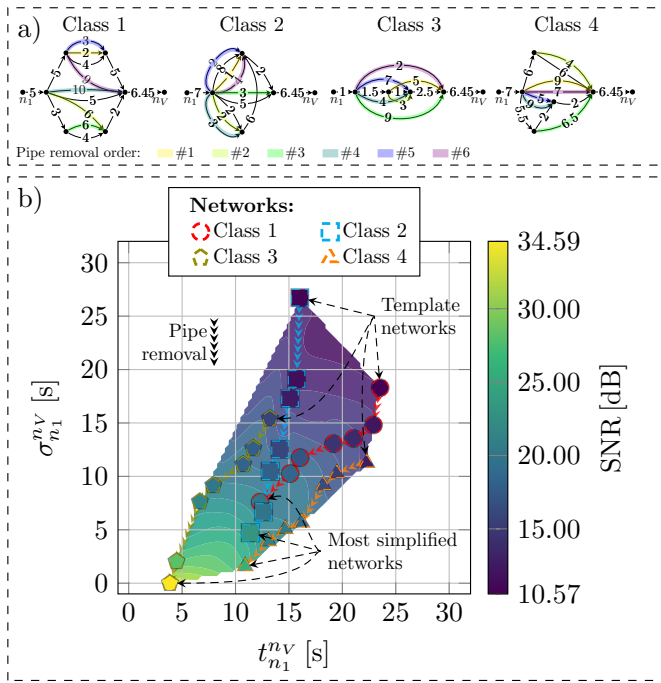


Fig. 4: Dispersion space filled with LBVNs. a) 28 networks are generated from four template LBVNs by removing one pipe per iteration in the indicated removal order. Pipe lengths in cm are given as edge weights, with $r = 1$ mm. b) Markers correspond to different LBVNs and color-code the SNR at the network outlets. The clear pattern between location in the space and SNR enables the characterization of the SNR based on the topology alone.

pipe lengths in unit cm are given as edge weights in Fig. 4a), with a radius of $r = 1$ mm. In each network, we simulate the instantaneous injection of $N = 2 \times 10^{12}$ SPIONs (as done in [6]) at a flow rate of $Q = 1 \times 10^{-7} \text{ m}^3 \text{ s}^{-1}$ and calculate the received SNRs as described in (16). Additionally, we map the networks within the dispersion space based on their topologies, with the SNRs color-coded and the removal of pipes indicated by arrow paths, cf. Fig. 4b). For the sake of visualization, we interpolate the SNR in the spaces between the networks.

Fig. 4b) reveals a strong correlation and clear pattern between the position of each LBVN in the space and its corresponding SNR, confirming our expectations from Section IV. Indeed, we find that networks exhibit systematically weaker SNRs with increasing $t_{n_1}^{n_V}$ and $\sigma_{n_1}^{n_V}$ due to enhanced dispersion, validating our choice of metrics. For example, the most simplified network from class 3 is the only LBVN with a single path from n_1 to n_V , resulting in $\sigma_{n_1}^{n_V} = 0$ and the highest SNR. Class 4 networks predominantly feature similar paths, leading to low $\sigma_{n_1}^{n_V}$, while the class 2 template exhibits paths of significantly different lengths, resulting in its simplifications being distributed across a wide range of $\sigma_{n_1}^{n_V}$. Despite these distinct class characteristics, our metrics capture the underlying topology-SNR relation.

VI. CONCLUSION

In this paper, we investigated how the topology of a LBVN affects the signal received at the outlet of the network. To allow quantitative statements, we introduced a generic end-to-end model for diffusion-advection-driven MC in LBVNs. The model extends an existing channel model to include turbulences induced at the injection site and at the branching points, and links it to a transparent RX model. We adapted the generic

model for communication using SPIONs to effectively isolate the effects topology imposes and to validate the end-to-end model with existing testbed data. Along with this, we presented a novel analytical model for the reception of SPIONs using a planar coil. Furthermore, we proposed two metrics, namely *molecule delay* and *multi-path spread*, that relate the network topology to molecule dispersion and thus to the SNR at the network outlet. This allows to characterize the received SNR solely based on the topology. Consequently, our framework can, e.g., aid optimal sensor placement in systems like the CVS under SNR constraints or predict branched testbed topologies that exhibit both structural complexity and reliable signal detection at the sensor.

Moving forward, we intend to further validate the SPION-based model with measurements from highly branched testbeds. Similarly, the modeling and comparison of other signaling molecule-RX pairs, e.g., based on ink particles or fluorescent proteins and spectral sensors, may be insightful.

REFERENCES

- [1] R. Mosayebi *et al.*, “Early cancer detection in blood vessels using mobile nanosensors,” *IEEE Trans. Nanobiosci.*, vol. 18, pp. 103–116, Apr. 2019.
- [2] C. Simo *et al.*, “Urease-powered nanobots for radionuclide bladder cancer therapy,” *Nat. Nanotechnol.*, vol. 19, pp. 554–564, Jan. 2024.
- [3] I. Akyildiz *et al.*, “The internet of bio-nano things,” *IEEE Commun. Mag.*, vol. 53, pp. 32–40, Mar. 2015.
- [4] Y. Chahibi *et al.*, “A molecular communication system model for particulate drug delivery systems,” *IEEE Trans. Biomed. Eng.*, vol. 60, pp. 3468–3483, Dec. 2013.
- [5] S. Pal, S. Misra, and N. Islam, “m-MSc: molecular communication-based analysis for controlled MSC treatment of cytokine storm,” *IEEE Trans. Mol. Biol. Multi-Scale Commun.*, vol. 9, pp. 286–294, Sep. 2023.
- [6] M. Bartunik *et al.*, “Channel parameter studies of a molecular communication testbed with biocompatible information carriers: methods and data,” *IEEE Trans. Mol. Biol. Multi-Scale Commun.*, vol. 9, pp. 489–498, Dec. 2023.
- [7] W. Wicke *et al.*, “Experimental system for molecular communication in pipe flow with magnetic nanoparticles,” *IEEE Trans. Mol. Biol. Multi-Scale Commun.*, vol. 8, pp. 56–71, Jun. 2022.
- [8] M. Bartunik *et al.*, “Planar coils for detection of magnetic nanoparticles in a testbed for molecular communication,” in *Proc. 9th ACM Int. Conf. Nanoscale Comput. Commun. (NANOCOM)*, Oct. 2022.
- [9] M. Schäfer *et al.*, “The chorioallantoic membrane model: a 3D in vivo testbed for design and analysis of MC systems,” *arXiv preprint arXiv:2406.09875*, 2024.
- [10] Y. Yu *et al.*, “Vascular network-inspired fluidic system (VasFluidics) with spatially functionalizable membranous walls,” *Nat. Commun.*, vol. 15 (1437), Feb. 2024.
- [11] S. Palanisamy and Y.-M. Wang, “Superparamagnetic iron oxide nanoparticulate system: synthesis, targeting, drug delivery and therapy in cancer,” *Dalton Trans.*, vol. 48, pp. 9490–9515, Jun. 2019.
- [12] F. T. M. Nieuwstadt, *Turbulence*, B. J. Boersma and J. Westerweel, Eds. Springer, 2016.
- [13] R. Aris, “On the dispersion of a solute in a fluid flowing through a tube,” *Proc. R. Soc. (London) A*, vol. 235, pp. 67–77, Apr. 1956.
- [14] M. Klarhöfer *et al.*, “High-resolution blood flow velocity measurements in the human finger,” *Magn. Reson. Med.*, vol. 45, pp. 716–719, Mar. 2001.
- [15] V. Jamali, A. Ahmadzadeh, and R. Schober, “On the design of matched filters for molecule counting receivers,” *IEEE Commun. Lett.*, vol. 21, pp. 1711–1714, Aug. 2017.
- [16] T. S. Rappaport, *Wireless Communications: Principles and Practice*. Cambridge University Press, Feb. 2024.